Supporting Information

Bound Oxygen-Atom Transfer Endowing Peroxidase-Mimic M-N-C with High Substrates Selectivity

Xinghua Chen,[a] Lufang Zhao,[a] Kaiqing Wu,[a] Hong Yang,[a] Qing Zhou,[a] Yuan Xu,[a] Yongjun Zheng,[b] Yanfei Shen,[b] Songqin Liu,[a] and Yuanjian Zhang*[a]

[a]Jiangsu Engineering Laboratory of Smart Carbon-Rich Materials and Device, Jiangsu Province Hi-Tech Key Laboratory for Bio-Medical Research, School of Chemistry and Chemical Engineering, Southeast University, Nanjing 211189, China, E-mail: Yuanjian.Zhang@seu.edu.cn

[b]Medical School, Southeast University, Nanjing 210009, China

Experiments

Materials.

o-Phenylenediamine (o-PD), ammonium persulfate (APS), iron(III) chloride hexahydrate ($FeCl_3 \cdot 6H_2O$), cobalt(II) chloride hexahydrate ($CoCl_2 \cdot 6H_2O$), manganese(II) chloride tetrahydrate ($MnCl_2 \cdot 4H_2O$), nickel(II) chloride hexahydrate ($NiCl_2 \cdot 6H_2O$), copper(II) chloride dihydrate ($CuCl_2 \cdot 2H_2O$), hydrochloric acid (HCl), hydrogen peroxide (H_2O_2, 30%), acetic acid (HAc), sodium acetate trihydrate ($NaAc \cdot 3H_2O$), sodium hydroxide (NaOH), dimethyl sulfoxide (DMSO) and ethanol were purchased from Sinopharm Chemical Reagent Co., Ltd. (China). Carbon black (CB, Ketjenblack EC 600 JD) was obtained from Akzo Nobel N.V. (Netherlands). Aminophthalhydrazide (luminol), mannitol and iron oxide (II, III) magnetic nanoparticles solution (Fe_3O_4, 100-300 nm, 25% in H_2O) were purchased from Aladdin Chemistry Co., Ltd. (China). 3,3',5,5'-tetramethylbenzidine (TMB), superoxide dismutase (SOD, from bovine erythrocytes, ≥3,000 units/mg protein) and peroxidase (HRP, from horseradish, ≥250 units/mg solid) were purchased from Sigma-Aldrich (USA). 5,5-dimethyl-1-pyrroline N-oxide (DMPO) and 2,2,6,6-Tetramethyl-4-piperidone hydrochloride (TEMP) were purchased from DOJINDO (Japan). Unless otherwise specified, all other chemicals were of analytical grade and used without further purification. Ultrapure water (18.2 MΩ cm) used in all the experiments was obtained from a Direct-Q 3 UV pure water purification system (Millipore, USA).

Synthesis of M-N-C nanozymes.

The M-N-C nanozymes were synthesized via a high-temperature pyrolysis, followed by an acid-etching. Taking preparation of $Fe_{0.5}$-N-C as an example, briefly, o-phenylenediamine (o-

PD, 3 g) and iron (III) chloride hexahydrate (0.5 g) were first stirred together with carbon black (CB, 1.5 g) in 1 M HCl (75 mL). The polymerization of o-PD was triggered by using ammonium persulfate (APS, 7.5 g) in an ice bath. The final Fe-N-C was obtained by pyrolyzing the precursor (3 g) at 900 ℃ under N_2 and acid-etching of metallic iron and iron oxide impurities by concentrated hydrochloric acid (30 mL). The other nanozymes with different transition metal species (i.e. Co, Mn, Ni, and Cu) and varied metal content (0.15 g, 0.5 g, 1.5 g and 4.5 g metal salts for $M_{0.15}$, $M_{0.5}$, $M_{1.5}$, $M_{4.5}$-N-C, respectively) were prepared similarly, and denoted as M_x-N-C, where M referred to the transition metal species and x was used to distinguish samples prepared with different metal content in the precursor. Unless otherwise specified, for clarity, the samples named M-N-C refers to $M_{0.5}$-N-C. As a control, the N-C without any metals was also synthesized under the identical conditions except for no adding of metal salts.

Characteristic of M-N-C nanozymes.

The scanning electron microscopy (SEM) images were obtained from a FEI Inspect F50 (FEI, USA). The transmission electron microscopy (TEM) and high-resolution transmission electron microscopy (HR-TEM) images were taken on a Tecnai G2 T20 (FEI, USA) and a JEM-2100 (JEOL, Japan) at an accelerating voltage of 200 kV. The N_2 adsorption−desorption (77 K) isotherms were measured by an Autosorb-iQ (Quantachrome, USA). The X-Ray diffraction (XRD) patterns were collected by an Ultima IV (Rigaku, Japan). The Raman spectra were performed on a DXR (Thermo Fisher, USA). The aberration-corrected high-angle annular dark field scanning transmission electron microscopy (AC HAADF-STEM) images were investigated by Themis Z (FEI, USA) equipped with energy-dispersive X-ray spectroscopy (EDS) mapping at an accelerating voltage of 300 kV. The X-ray photoelectron spectroscopy

(XPS) was carried out on an ESCALAB 250XI electron spectrometer (Thermo Fisher, USA) with monochromatic Al Kα X-rays (hν = 1486.6 eV) as the excitation source, and the peak positions were corrected by the C 1s peak at 284.6 eV. The X-ray adsorption fine structure (XAFS) spectra were obtained at 1W1B station in BSRF (Beijing Synchrotron Radiation Facility, China) operated at 2.5 GeV with a maximum current of 250 mA. The UV-Vis absorption spectra were recorded by a Cary 100 UV-is (Agilent, Singapore). The time-dependent light intensity spectra were measured with a QE Pro spectrometer (Ocean Optics, USA). The generated oxygen was measured by an oxygen electrode on JPSJ-605 (Leici, China). The photographs were acquired using a D7100 digital camera (Nikon, Japan). The electron paramagnetic resonance (EPR) spectra were taken on EMX-10/12 (Bruker, Germany).

Peroxidase-like activity and kinetic assay of M-N-C nanozymes.

The catalytic oxidation of TMB with H_2O_2. The activity of M-N-C for catalyzing the oxidation of TMB with H_2O_2 was assessed by monitoring the time dependent absorbance (at 652 nm for the TMB_{ox}) change via the kinetic mode using a Cary 100 UV-vis spectrometer (Agilent, Singapore). Typically, the M-N-C nanozyme (2 mg mL^{-1}, 10 μL) was added firstly into 0.1 M HAc-NaAc buffer solution (pH 3.6, 990 μL) containing TMB (100 mM in DMSO, 10 μL) and H_2O_2 (10 M, 10 μL), then the test was started quickly at room temperature. The initial reaction velocity was calculated as follow:

$$\nu = \frac{\Delta A / \Delta t}{\varepsilon \times l} \quad (1)$$

Where ν is initial reaction velocity, $\Delta A/\Delta t$ is the initial rate of change in absorbance at 652 nm s^{-1}, ε is the molar absorption coefficient of TMB ($\varepsilon_{652\ nm}$ = 39,000 $M^{-1}\ cm^{-1}$), and l is the path length of light traveling in the cuvette (l = 0.2 cm).

The steady-state kinetic assay of $Fe_{0.5}$-N-C was performed under above condition with varied volume of TMB (0, 1 ,2, 4, 6, 10, 15, 20, 30, 40 μL) or H_2O_2 (0, 0.5, 1, 2, 4, 6, 8, 10, 20 μL) solution, respectively. The Michaelis-Menten constant (e.g. K_m and ν_{max}) was calculated as follow based on the Michaelis-Menten saturation curve:

$$\nu = \frac{\nu_{max} \times [S]}{K_m + [S]} \quad (2)$$

Where ν is the initial reaction velocity, ν_{max} is the maximal reaction rate that is observed at saturated substrate concentration, [S] is the concentration of the substrate and K_m is the Michaelis constant. In addition, the experiments under different pH (4.5 and 5.5) and temperature (37 ℃ and 60 ℃) were also investigated in the same method for $Fe_{0.5}$-N-C.

The specific activity (SA) of $Fe_{0.5}$-N-C, defined as activity units per milligram of nanozyme, was carried out at the simlar condition with a series of $Fe_{0.5}$-N-C dosage (2.5, 5, 7.5, 10, 12.5, 15 μL). One unit is defined as the amount of nanozyme that catalytically produces 1 μmol of product per minute at standard condition. The SA was obtained by the following formula:

$$SA = \frac{V \times \nu}{[m]} \quad (3)$$

Where SA is the specific activity expressed in units per milligram (U mg^{-1}), V is the total volume of reaction solution (μL), ν is initial reaction velocity (μM min^{-1}), and [m] is the nanozyme weight (mg) of each assay.

The Michaelis–Menten constant was obtained based on the Michaelis–Menten saturation curve using GraphPad Prism 8.4.3 (GraphPad Software).

The catalytic oxidation of Luminol with H_2O_2. The activity of M-N-C for catalyzing the oxidation of Luminol with H_2O_2 was investigated by monitoring the time dependent chemiluminescent (CL) emission intensity (typically maximized at 425 nm for luminol) by using the timing diagram mode

of a QE Pro spectrometer (Ocean Optics, USA). Briefly, M-N-C nanozyme (2 mg mL^{-1}, 50 μL), H_2O_2 (10 M, 10 μL) and luminol (0.1 M, 50 μL) was added successively into 0.01 M NaOH (1850 μL) under stirring at room temperature after the timing diagram mode was started. For Co-N-C, the temperature (0-60 ℃) dependent activity of the catalytic oxidation of luminol with H_2O_2 was also investigated in the similar condition.

Free radical identification.

The reactive oxygen species (ROS) participated in the oxidation of TMB and Luminol were investigated by comparing the reactivity in the absence or presence of ROS scavengers (SOD and mannitol scavenges superoxide and hydroxyl radical, respectively). In the catalytic oxidation of TMB, the M-N-C nanozyme (2 mg mL^{-1}, 5 μL) was added firstly into 0.1 M HAc-NaAc buffer solution (pH 3.6, 995 μL) containing SOD (2 mg mL^{-1}, 10 μL; or 10 μL, 1 M mannitol), TMB (0.1 M in DMSO, 5 μL) and H_2O_2 (1 M, 5 μL) then the test was started quickly at room temperature. In the catalytic oxidation of Luminol, SOD (2 mg mL^{-1}, 50 μL; or 50 μL, 1 M mannitol), M-N-C nanozyme (2 mg mL^{-1}, 50 μL), H_2O_2 (10 M, 10 μL) and luminol (0.1 M, 50 μL) was added successively into 0.01 M NaOH (1800 μL) under stirring at room temperature after the timing diagram mode was started.

The EPR spectra were taken to further explore the ROS generated during the activation of H_2O_2 by the Fe-N-C, Fe_3O_4 and HRP. 5,5-dimethyl-1-pyrroline N-oxide (DMPO) and 2,2,6,6-Tetramethyl-4-piperidone hydrochloride (TEMP) were adopted to trap the short-lived hydroxyl radical (superoxide radical was trapped in methanol solution) and singlet oxygen in 0.1 M HAc-NaAc aqueous solution, respectively. Typically, the catalysts (0.4 mg mL^{-1}, 10 μL; 2 mg mL^{-1} for Fe_3O_4 considering the much lower catalytic activity of Fe_3O_4 than that for Fe-N-C) was added into 0.1 M HAc-NaAc buffer solution (pH 3.6 , 190 μL) containing DMPO (2 M, 10 μL; 0.4 M for TEMP) and H_2O_2 (1 M, 10 μL) first and then the test was started at room

temperature. The EPR spectra of blank references were also obtained by the same method except that neither catalysts or H_2O_2 were added.

Catalase-like activity of M-N-C nanozyme.

The catalase-like property of $M_{0.5}$-N-C (M=Fe, Co) was studied by measuring the produced oxygen via an oxygen electrode on JPSJ-605 (Leici, China) in 0.1 M HAc-NaAc buffer and 0.01 M NaOH. Briefly, H_2O_2 (10 M, 0.02 mL) was added into the buffer solution (9.98 mL) containing $M_{0.5}$-N-C (2 mg mL^{-1}, 0.01 mL, or absence of nanozyme for control) under stirring at room temperature and the dissolved oxygen concentration (mg L^{-1}) was recorded at different time. The influence of TMB and Luminol on the decomposition of H_2O_2 catalyzed by $M_{0.5}$-N-C were carried out at the identical conditions except that the buffer solution also contains TMB (0.1 M, 0.1 mL) and Luminol (0.1 M, 0.1 mL) in 0.1 M HAc-NaAc buffer and 0.01 M NaOH, respectively.

Computational Methods and Models.

The density functional theory (DFT) calculations were implemented by using the Vienna Ab-initio Simulation Package (VASP) code.[1-4] For the total energy calculations, the plane wave cutoff energy was 400 eV. Ion–electron interactions were represented by ultrasoft pseudopotentials within the framework of the projector-augmented wave (PAW) method.[5] The generalized gradient approximation (GGA) with the Perdew-Burke-Ernzerhof (PBE) functional was adopted as the exchange-correlation functional.[5, 6] The Brillouin zone integration was approximated by a sum over special selected k-points using the 2×2×1 MonkhorstPack method.[7] The geometries were optimized until the energy was converged to 1×10^{-5} eV/atom and the forces to 0.02 eV/Å. The vacuum region was set to 15 Å in the z direction to separate the slabs to eliminate the interactions between modeled system. The

M-N-C (M = Fe, Co) was modeled by p (5×5) supercell. The acid and alkaline system were modelled by adsorbing one hydrogen atom and hydroxyl on metal atom, respectively.

The adsorption energies (E_{ads}) of species were defined according to the equation (4):

$$E_{\mathrm{ads}} = E_{\mathrm{total}} - E_{\mathrm{catalyst}} - E_{\mathrm{species}} \quad (4)$$

Where E_{total} is the total energies of the adsorbed system, E_{catalyst} is the energy of the catalyst, and E_{species} represents the energy of species in the gas phase.

The activation barrier (E_{a}) and reaction energy (ΔH) were calculated according to the equations (5) and (6):

$$E_a = E_{\mathrm{TS}} - E_{\mathrm{R}} \quad (5)$$

$$\Delta H = E_{\mathrm{P}} - E_{\mathrm{R}} \quad (6)$$

Where E_{R}, E_{TS} and E_{P} correspond to the total energies of the slab along with adsorbed reactant, the transition state and the product, respectively.

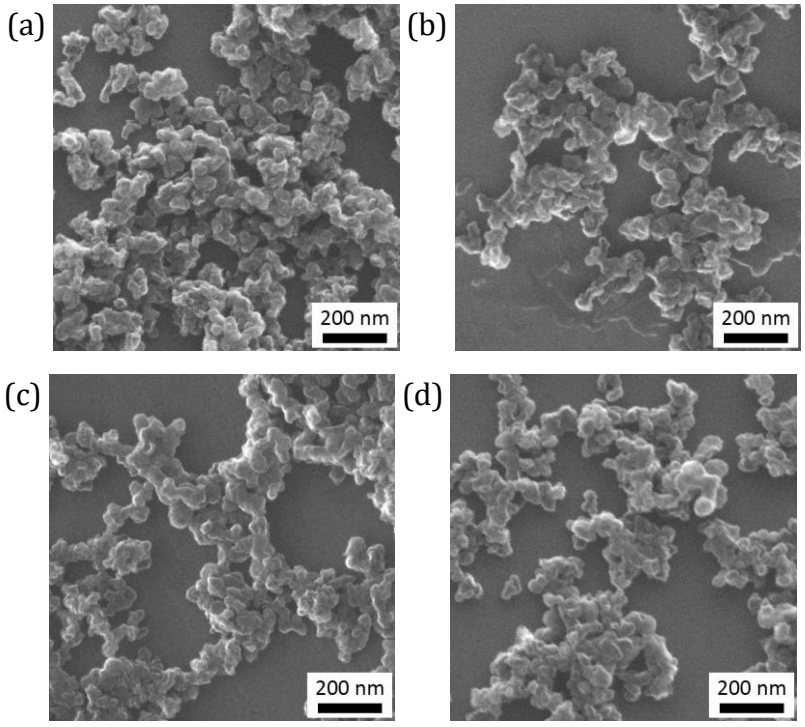

Figure S1. SEM images of $Fe_{0.5}$-N-C (a), $Fe_{0.15}$-N-C (b), $Fe_{1.5}$-N-C (c) and metal free N-C (d) nanozymes.

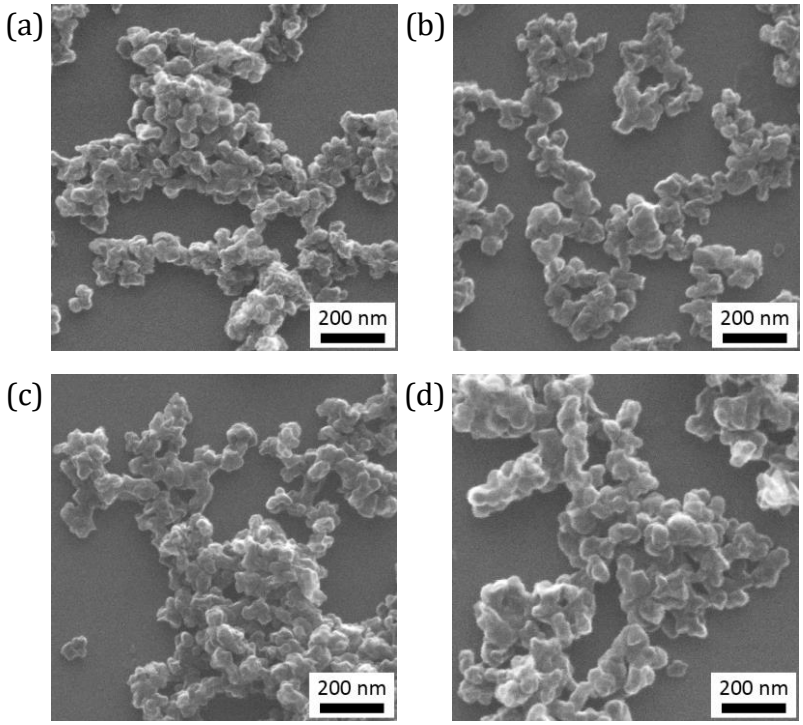

Figure S2. SEM images of Mn-N-C (a), Co-N-C (b), Ni-N-C (c) and Cu-N-C (d). Their size and shape did not significantly rely on the type of metal.

As the size and morphology of nanozymes may influence their activity,[8, 9] the negligible variation of these structures would simply the disclosure of structure-properties relationship for M-N-C nanozymes.

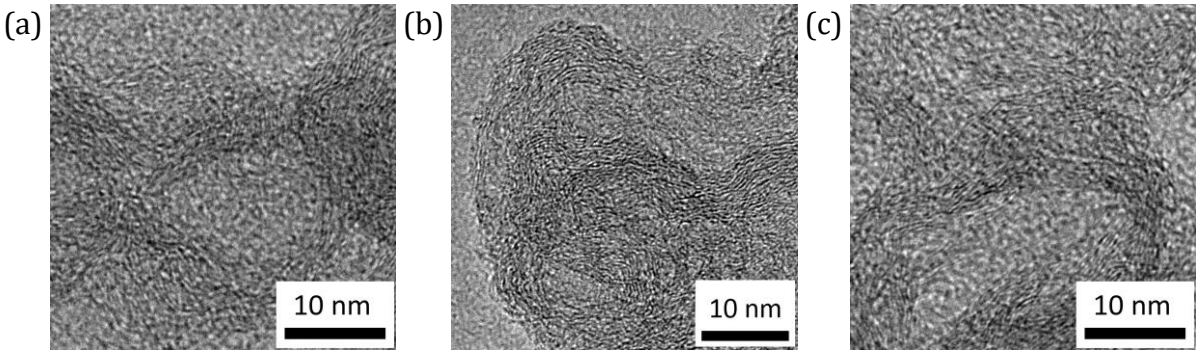

Figure S3. High-resolution TEM images of $Fe_{0.5}$-N-C (a), $Fe_{1.5}$-N-C (b) and $Fe_{4.5}$-N-C (c) nanozymes.

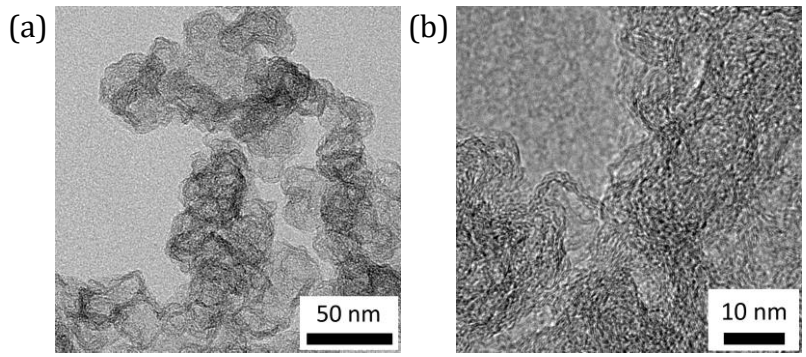

Figure S4. TEM (a) and high-resolution TEM (b) images of CB. CB support was composed with typical turbostratic multilayer of graphite domains.

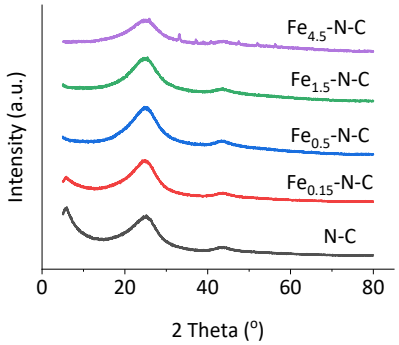

Figure S5. X-ray powder diffraction spectra of N-C and all the Fe_x-N-C nanozymes.

To better understand the graphitic structures of M-N-C, the powder X-ray diffraction (XRD) patterns were measured. For instance, a broad (002) peak indicating the anarchy of layer stacking was observed in the XRD pattern of $Fe_{0.5}$-N-C (**Figure S5**), consistent with the HR-TEM images (**Figure S3**). As no obvious peaks of crystallized iron-related species were observed, iron was supposed to exist at the atomic level. By moderate increase of the iron concentration, the (002) peak was practically not affected, but some weak crystallized iron and iron sulfide were noticed in an extreme case, i.e. $Fe_{4.5}$-N-C (**Figure S5**). It suggested that a proper moderate metal concentration was essential herein for the preparation of uniformly dispersed nanocomposites.

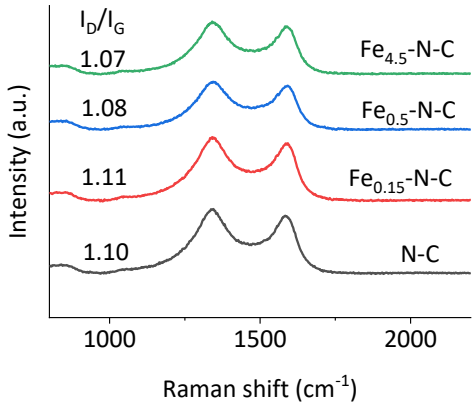

Figure S6. Raman spectra of N-C and all the Fe_x-N-C nanozymes.

The Raman spectrum of $Fe_{0.5}$-N-C typically exhibited D band (ca. 1350 cm^{-1}) and G band (ca. 1580 cm^{-1}), which indicating the carbon disorder and crystallization, respectively.[10] The high intensity ratio of D-to-G band (I_D/I_G) confirmed again the disorder in graphene basal planes,[10] and it is negligibly influenced by the iron concentration.

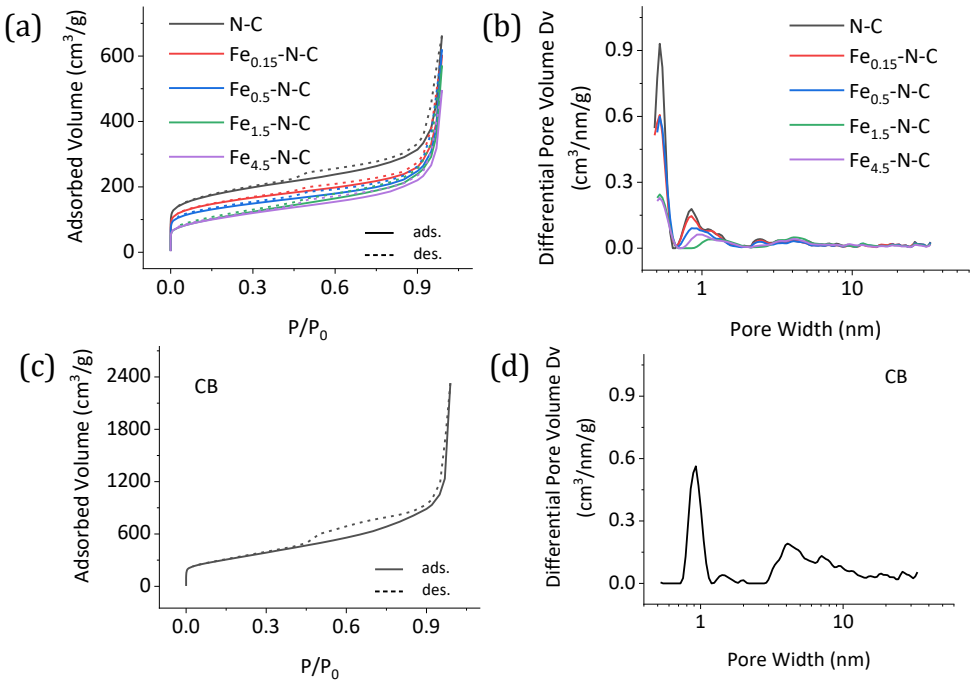

Figure S7. N_2 adsorption and desorption isotherms (a, c) and pore size distribution (imitated using QSDFT; b, d) of N-C (a, b), all the Fe_x-N-C (a, b) and CB (c, d) nanozymes.

The N_2 sorption isotherms of Fe-N-C (**Figure S7a**) featured a typical micropore and negligible mesopore, determined by the high adsorption capacity in the ultralow pressure zone and the unobvious hysteresis, respectively. The pore size distribution analysis using a quenched solid density functional theory (QSDFT, **Figure S7b**) demonstrated a typical texture with a majority of micropores (ca. 0.5-2 nm) and a small fraction of mesopores (ca. 2-6 nm). In addition, the micropore size was gradually narrowing with the increase of iron content except for $Fe_{4.5}$-N-C. The phenomena of micropore size shrinking with increasing iron content might be due to the formation of carbon-supported N-coordinated iron in the micropores. Conditions outside the law might be due to the impact of acid-etching crystal iron phase. The N_2 sorption isotherms (**Figure S57c**) and the pore size (QSDFT, **Figure S7d**) of CB demonstrated a typical texture with micropores (ca. 0.7-2 nm) and mesopores (ca. 3-12 nm). These pores were much smaller than the diameter of the particle cavity observed by TEM images, indicative of a closed turbine-like graphite shell layer.

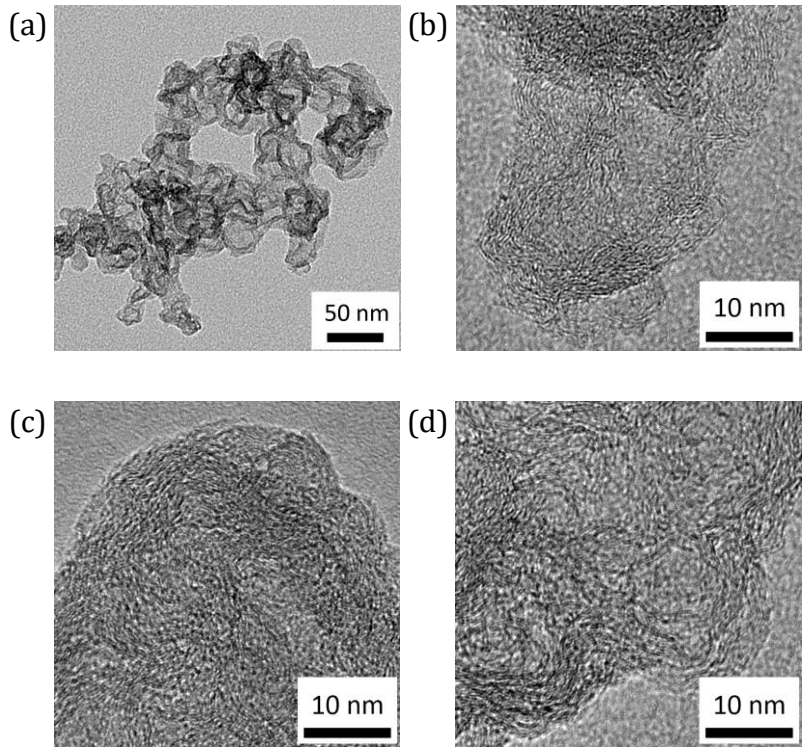

Figure S8. TEM (a) and high-resolution TEM (b) images of $Co_{0.5}$-N-C. HR-TEM images of $Co_{1.5}$-N-C (c) and $Co_{4.5}$-N-C (d) nanozymes.

As can be seen, all the Co_x-N-C nanozymes were composed turbostratic multilayer of graphite domains.

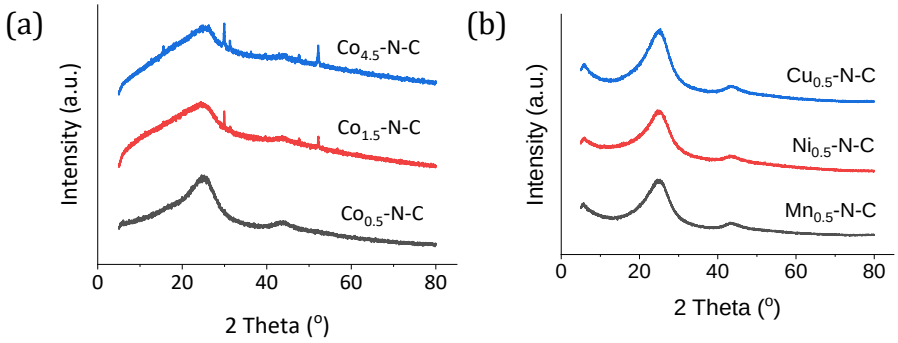

Figure S9. X-ray powder diffraction spectra of Co_x-N-C (a) and $M_{0.5}$-N-C (M=Mn, Ni and Cu, b).

A broad (002) peak indicating the anarchy of layer stacking was observed in the XRD pattern of $Co_{0.5}$-N-C (**Figure S9a**), which was consistent with the HR-TEM images. And no peaks of crystallized cobalt were appeared. By increase of the cobalt concentration, the (002) peak was practically not affected, but some weak crystallized cobalt were noticed in $Co_{1.5}$-N-C and $Co_{4.5}$-N-C. It suggested that a proper moderate metal concentration was essential herein for the preparation of uniformly dispersed nanocomposites. The XRD pattern of the other $M_{0.5}$-N-C (M = Mn, Ni, and Cu, see **Figure S9b**) also featured the typical disordered carbon and no peaks of metal species.

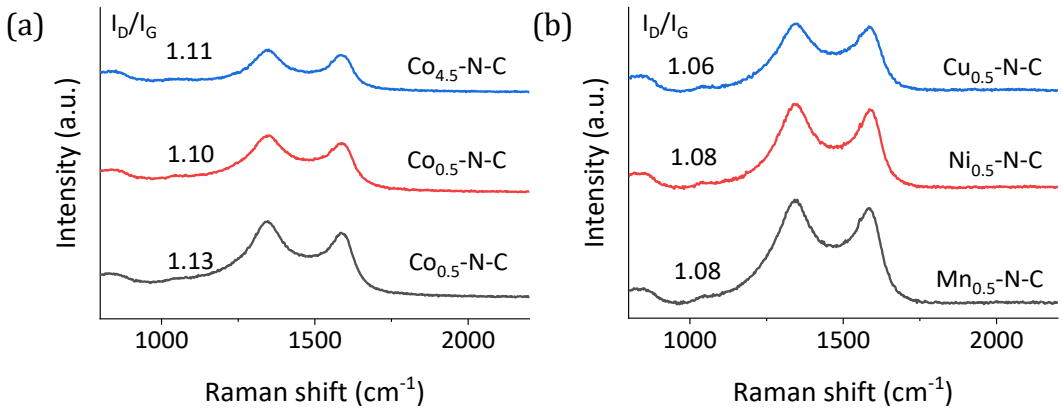

Figure S10. Raman spectra of all the Co_x-N-C (a) and $M_{0.5}$-N-C (M=Mn, Ni and Cu; b) nanozymes.

The Raman spectrum of all the Co-N-C (**Figure S10a**) and $M_{0.5}$-N-C (M=Mn, Ni and Cu; **Figure S10b**) also typically exhibited D band (ca. 1350 cm^{-1}) and G band (ca. 1580 cm^{-1}. The high intensity ratio of D-to-G band (I_D/I_G) confirmed again the disorder in graphene basal planes,[10] and it is negligibly influenced by the cobalt concentration and the type of metals.

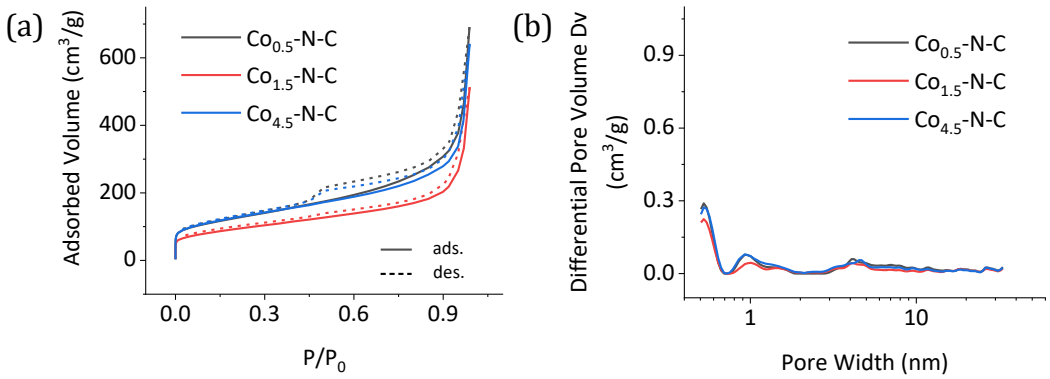

Figure S11. N_2 adsorption and desorption isotherms (a) and pore size distribution (imitated using QSDFT; b) of Co_x-N-C nanozymes.

The N_2 sorption isotherms (**Figure S11a**) and the pore size distribution of Co-N-C (QSDFT, **Figure S11b**) demonstrated a typical texture with a majority of micropores (ca. 0.5-2 nm) and a small fraction of mesopores (ca. 2-6 nm). The phenomena of micropore size shrinking with increasing cobalt content and the special case for $Co_{4.5}$-N-C was similar with that for Fe-N-C.

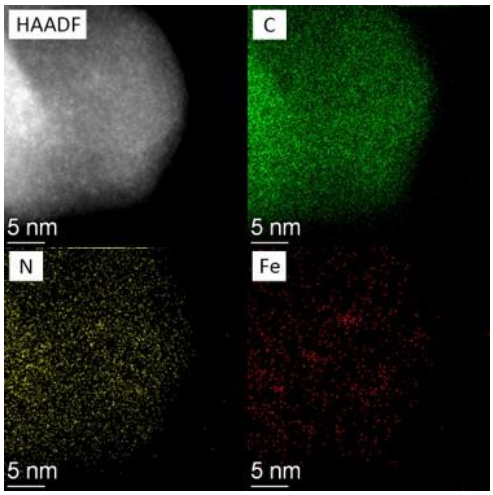

Figure S12. The corresponding element mapping images of Fe-N-C.

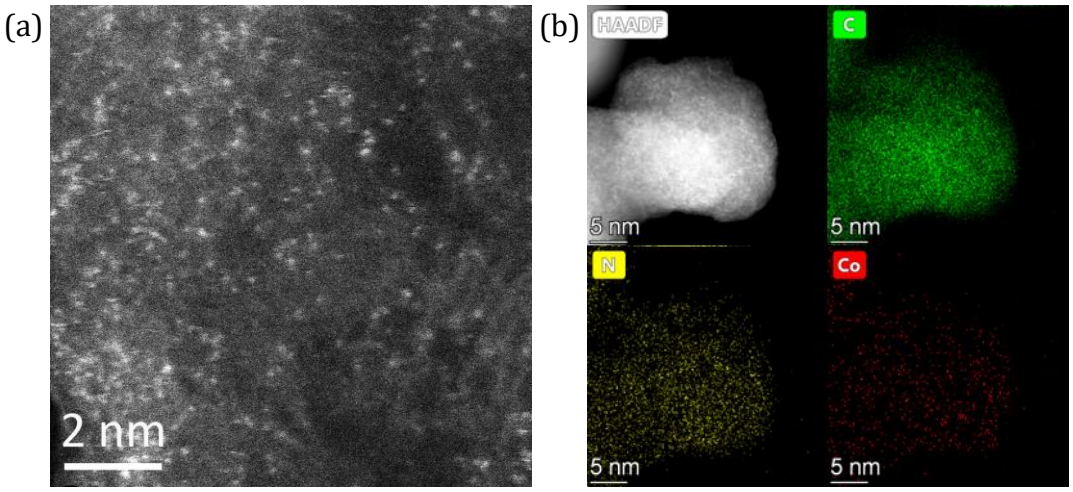

Figure S13. HAADF-SETM image (a) and the corresponding element mapping images (b) of Co-N-C.

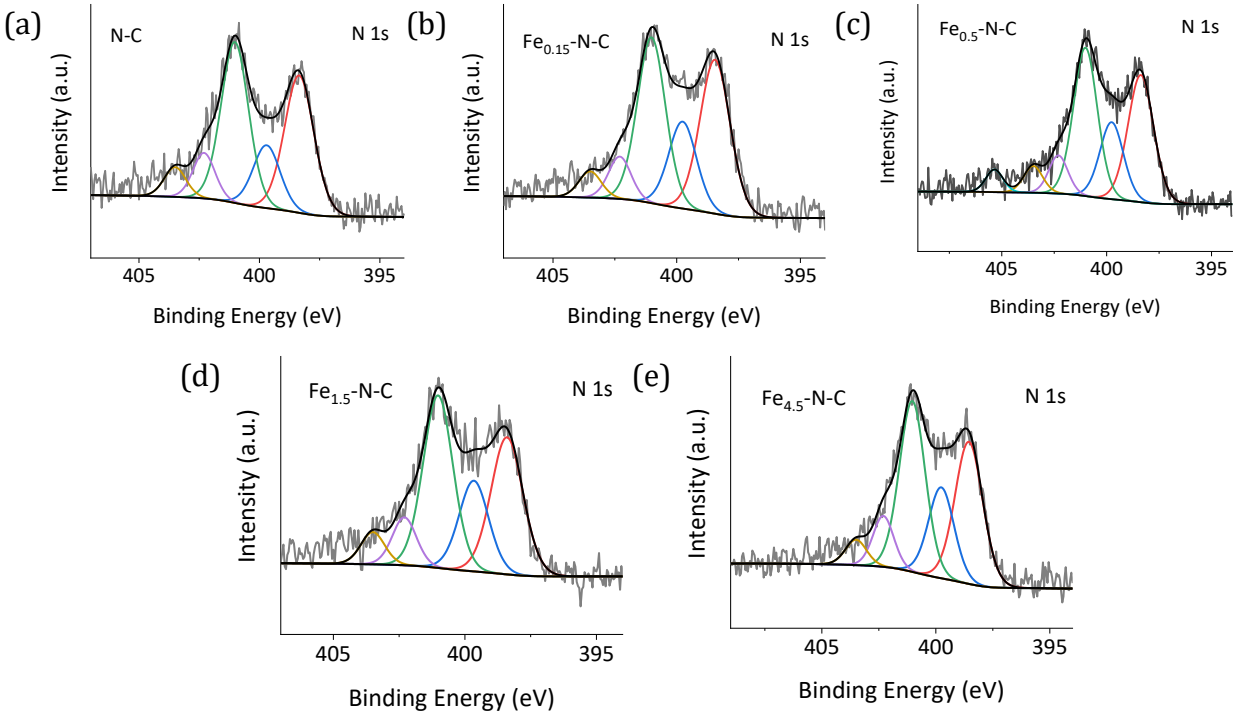

Figure S14. Deconvoluted high-resolution N 1s spectra of N-C (a), $Fe_{0.15}$-N-C (b), $Fe_{0.5}$-N-C (b), $Fe_{1.5}$-N-C (c) and $Fe_{4.5}$-N-C (d) nanozymes.

The high-resolution N 1s spectra of N-C and all Fe-N-C nanozymes could be deconvoluted into porphyrin-like Fe-N coordination and/or imide (399.7 eV), as well as pyridinic- (398.3 eV), pyrrolic- (401 eV), graphitic- (402.3 eV), and oxidized- (403.5 eV) N species. To further prove that Fe-N coordination was existed in $Fe_{0.5}$-N-C, the N species centered at 399.7 eV of N-C and $Fe_{0.15}$-, $Fe_{1.5}$-, $Fe_{4.5}$-N-C nanozymes were analyzed. As shown in **Figure S14** and **Table S2**, N species centered at 399.7 eV was existed both in N-C and all the Fe_x-N-C. However, it was noteworthy that the percentage of N species centered at 399.7 eV of $Fe_{0.5}$-N-C (18.49 %) was significantly higher than that of N-C (14.45 %) and gradually increased with Fe content (18.88 and 18.99 % for $Fe_{0.15}$-, $Fe_{4.5}$-N-C, respectively), indicating that Fe-N coordination structure were formed in Fe-N-C.

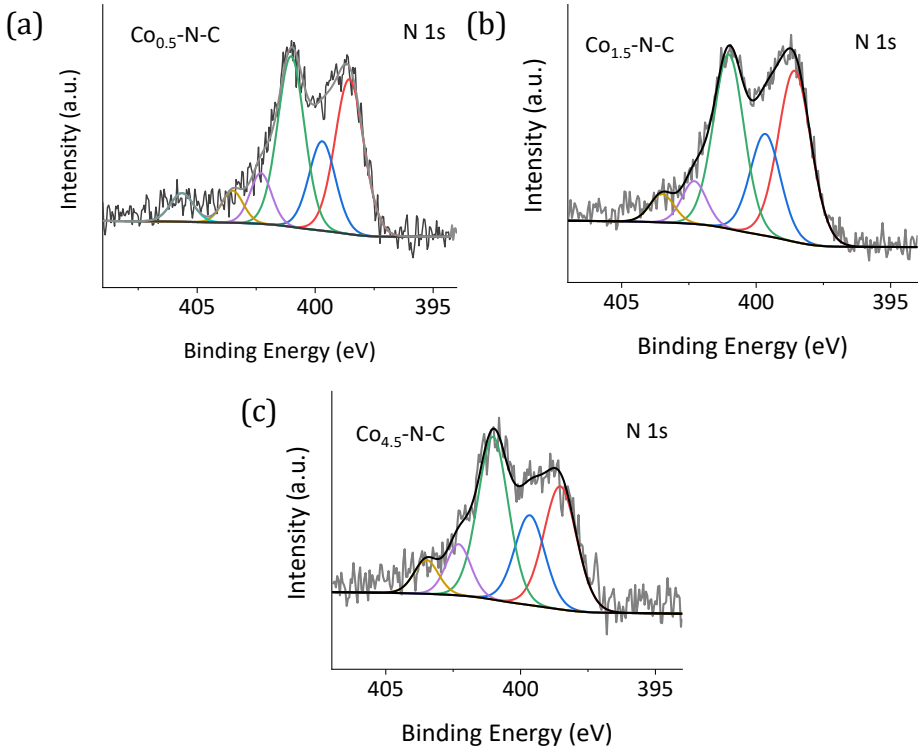

Figure S15. Deconvoluted high-resolution N 1s spectra of $Co_{1.5}$-N-C (a) and $Co_{4.5}$-N-C (b) nanozymes.

The high-resolution N 1s spectra of all Co-N-C nanozymes could also be deconvoluted into porphyrin-like Fe-N coordination and/or imide (399.7 eV), as well as pyridinic- (398.3 eV), pyrrolic- (401 eV), graphitic- (402.3 eV), and oxidized- (403.5 eV) N species. The further investigation of N species centered at 399.7 eV (**Figure S15** and **Table S2**) shown that the percentage of this N species of $Co_{0.5}$-N-C (18.04 %) was also significantly higher than that of N-C (14.45 %) and gradually increased with Co content (19.58 and 19.72 % for $Co_{1.5}$-, $Co_{4.5}$-N-C, respectively), revealing that Co-N coordination structure were formed in Co-N-C and the content of Co-N species could be improved by moderately increasing the concentration of cobalt salts in the precursor.

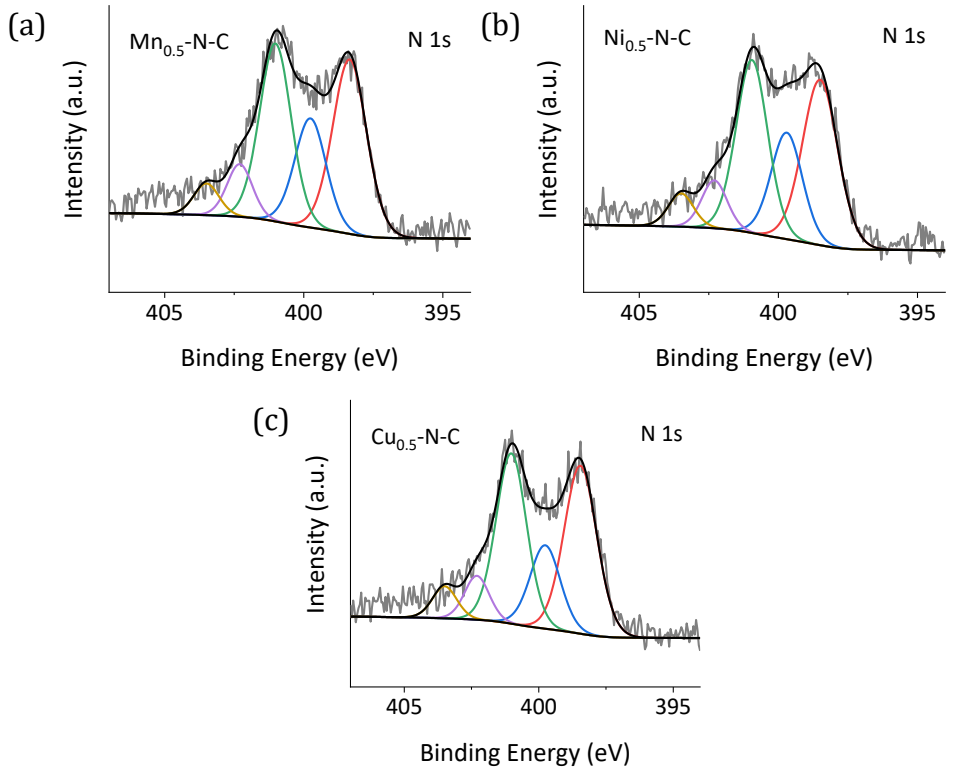

Figure S16. Deconvoluted high-resolution N 1s spectra of $Mn_{0.5}$-N-C (a), $Ni_{0.5}$-N-C (b) and $Cu_{0.5}$-N-C (c) nanozymes.

The high-resolution N 1s spectra of the other M-N-C (M = Mn, Ni and Cu) nanozymes (**Figure S16**) could also be deconvoluted into porphyrin-like Fe-N coordination and/or imide (399.7 eV), as well as pyridinic- (398.3 eV), pyrrolic- (401 eV), graphitic- (402.3 eV), and oxidized- (403.5 eV) N species. The percentage of this N species centered at 399.7 eV (**Table S2**) of $Mn_{0.5}$-N-C (20.03 %), $Ni_{0.5}$-N-C (20.01 %) and $Cu_{0.5}$-N-C (16.76 %) was also significantly higher than that of N-C (14.45 %).

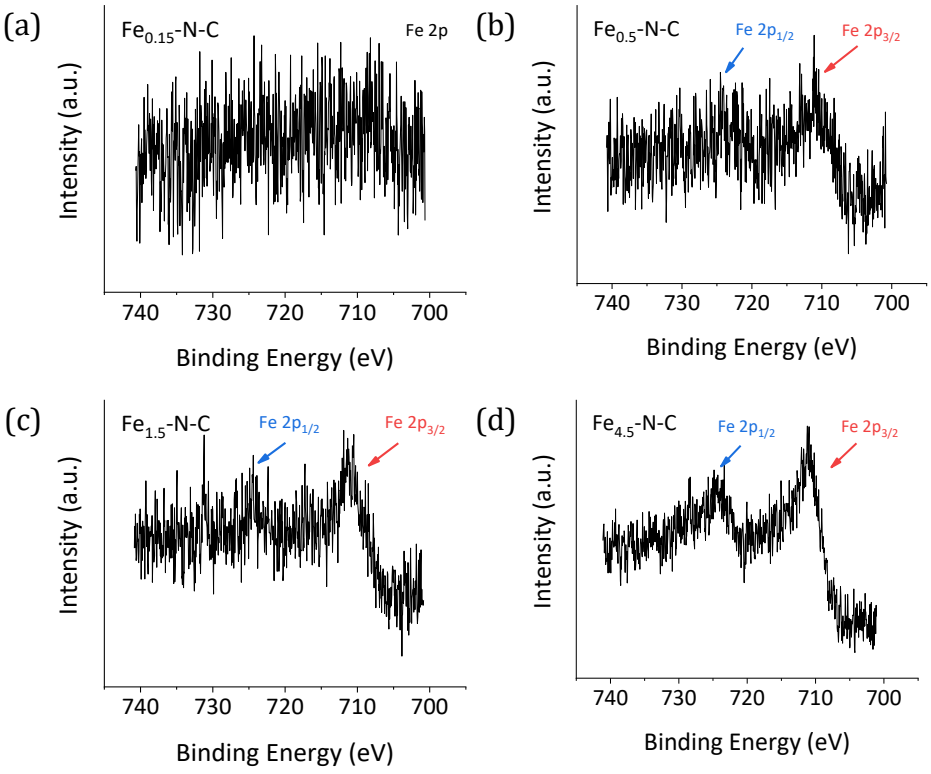

Figure S17. High-resolution Fe 2p spectra of all the Fe_x-N-C nanozymes.

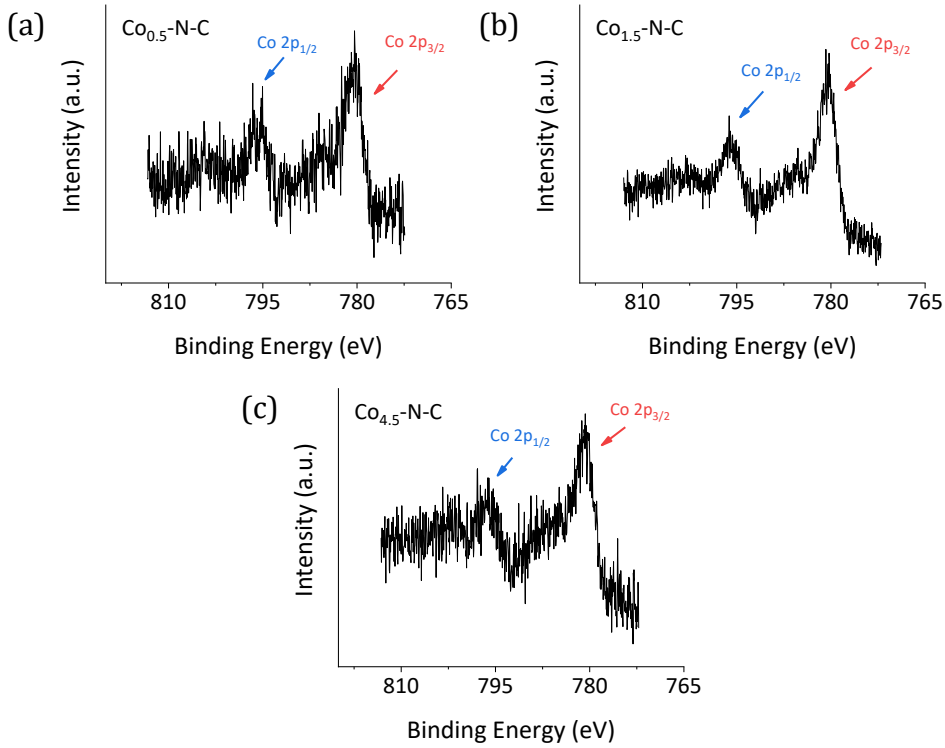

Figure S18. High-resolution Co 2p spectra of all the Co_x-N-C nanozymes.

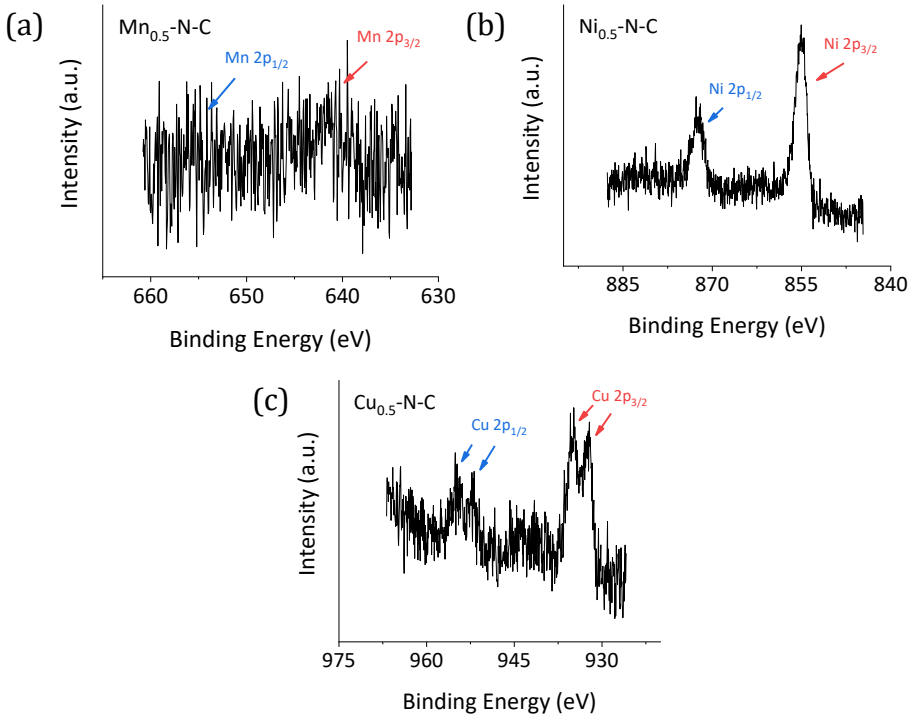

Figure S19. High-resolution Mn (a), Ni (b) and Cu (c) 2p spectra of $M_{0.5}$-N-C (M=Mn, Ni and Cu) nanozymes.

The high-resolution metal 2p spectra of all M-N-C except for $Fe_{0.15}$-N-C can be well divided into two regions of high and low energy assigned to the $2p_{1/2}$ and $2p_{3/2}$ regions, respectively. The inapparent 2p spectra $Fe_{0.15}$-N-C presumably due to the low doping content.

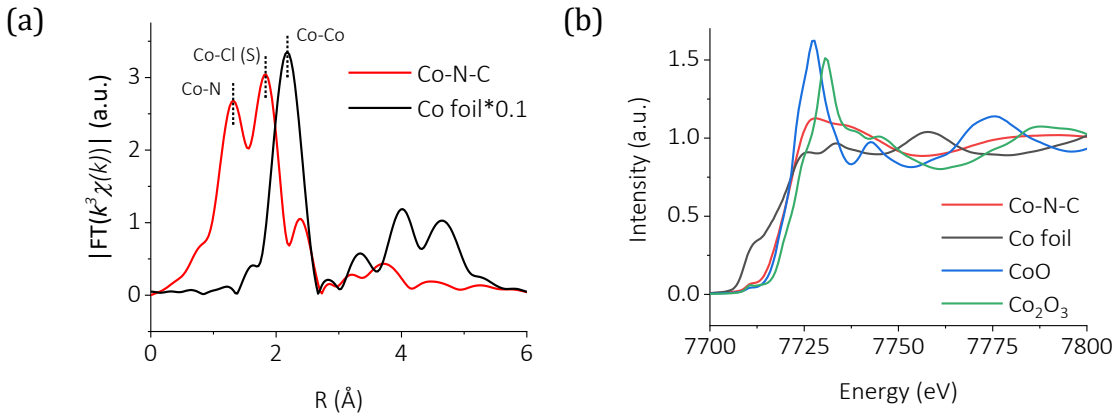

Figure S20. Fourier transformed k^3-weighted EXAFS spectra (c) and XANES spectra (d) of Co-N-C and the reference samples at Co K-edge.

As shown in **Figure S20**, no Co-Co scattering path (ca. at 2.18 Å) was observed in $Co_{0.5}$-N-C, indicating the single Co sites. Two main peaks centered ca. at 1.31 Å and 1.82 Å, attributing to Co-N and Co-Cl (S) scattering path, respectively, were existed, which was different from the coordination sate of Fe sites in $Fe_{0.5}$-N-C. The Co^{2+} was confirmed by the absorption edge position of $Co_{0.5}$-N-C and the referenced CoO and Co_2O_3.

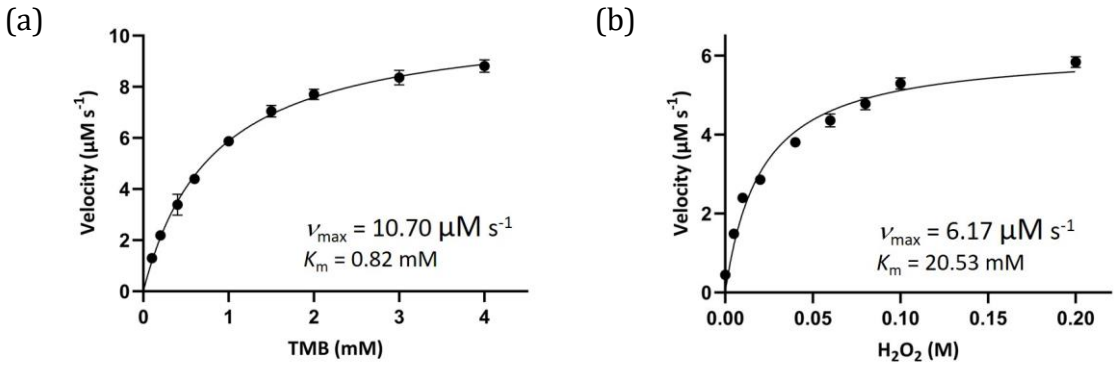

Figure S21. The typical Michaelis-Menten curves for 20 μg/mL $Fe_{0.5}$-N-C with TMB (a; [H_2O_2]: 0.1 M) and H_2O_2 (b; [TMB]: 1 mM) as substrate in 0.1 M HAc-NaAc (pH 3.6), respectively.

The steady-state kinetic of $Fe_{0.5}$-N-C was also estimated, a typical Michaelis-Menten kinetic dominated catalytic oxidation of TMB using H_2O_2. The Michaelis-Menten constant (K_m) value of $Fe_{0.5}$-N-C was 0.82 mM for TMB and 20.53 mM for H_2O_2 and the maximum initial velocity (V_{max}) value of $Fe_{0.5}$-N-C for TMB was 10.70 μM/s.

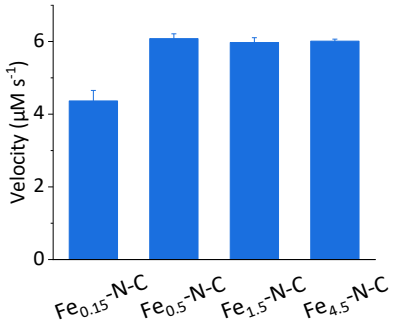

Figure S22. The initial velocity of catalytic oxidation of 1 mM TMB with 100 mM H_2O_2 in the presence of 20 μg/mL of Fe_x-N-C nanozymes in 0.1 M HAc-NaAc (pH 3.6).

The catalytic activity of Fe-N-C can be regulated by the iron content in the precursor. With increasing the iron content, the activity of Fe-N-C increases ($Fe_{0.15}$-N-C: 4.36 μM/s, $Fe_{0.5}$-N-C: 6.08 μM/s) and reached a plateau ($Fe_{1.5}$-N-C: 5.97 μM/s, $Fe_{4.5}$-N-C: 6.01 μM/s), which presumably due to the existence of a maximum M-N_x doping.

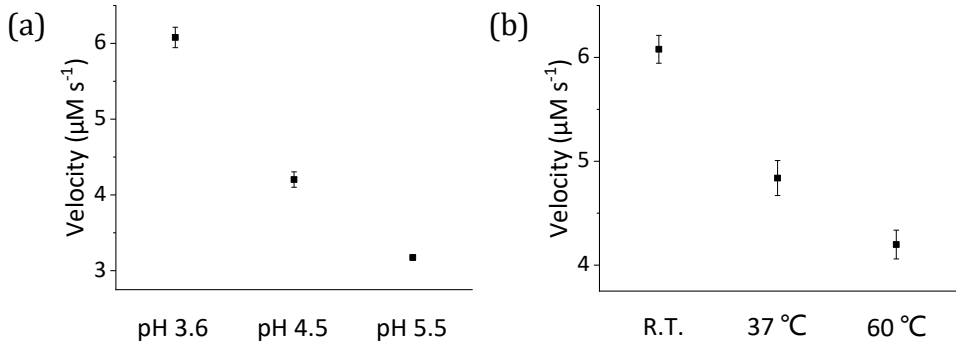

Figure S23. The pH (a) and temperature (b) dependent activity of the catalytic oxidation of 1 mM TMB with 100 mM H_2O_2 in the presence of 20 μg/mL Fe-N-C nanozyme.

Other factors, such as pH and temperature, that closely associated with the catalytic activity of natural peroxidase were investigated. It was observed that the catalytic activity of Fe-N-C obeyed the pH and temperature dependent manner within the scope of the investigation.

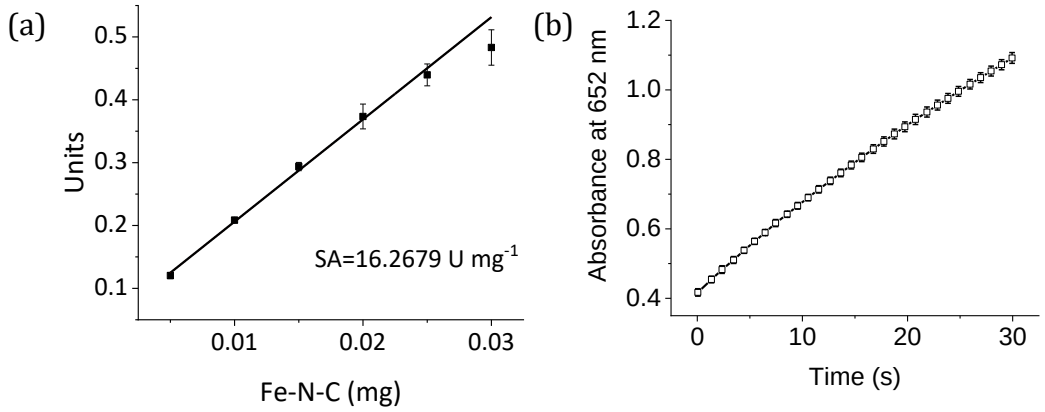

Figure S24. (a) The specific activity of Fe-N-C calculated using the nanozyme activity standardization method. [TMB]: 1 mM; [H_2O_2]: 100 mM; (b) Kintic curves of $A_{652\ nm}$ for monitoring the catalytic oxidation of 1 mM TMB with 100 mM H_2O_2 in the presence of 10 μg mL^{-1} Fe-N-C.

The specific activity of Fe-N-C, defined as activity units per milligram of nanozyme, was calculated as 16.27 U/mg using the nanozyme activity standardization method (**Figure S24a**).[11] The catalytic activity of peroxidase mimic can also be obtained from the kinetic curves of TMB oxidation. For a fair comparison, we adopted the same conditions as that was used in the literature.[12] In regard of absorbance of TMB_{ox} at 30 s, the peroxidase-like activity of Fe-N-C (**Figure 24b**, Absorbance: 1.09) was much higher than all of these typical nanozymes (**Ref. S8,** the highest Absorbance: 0.55). Thus the peroxidase-like activity of Fe-N-C competitive to the state-of-the-art peroxidase-mimicking nanozymes, which demonstrated the merits of single atom configuration and the surface-confined intermediates (see more discussion in the following text).[13]

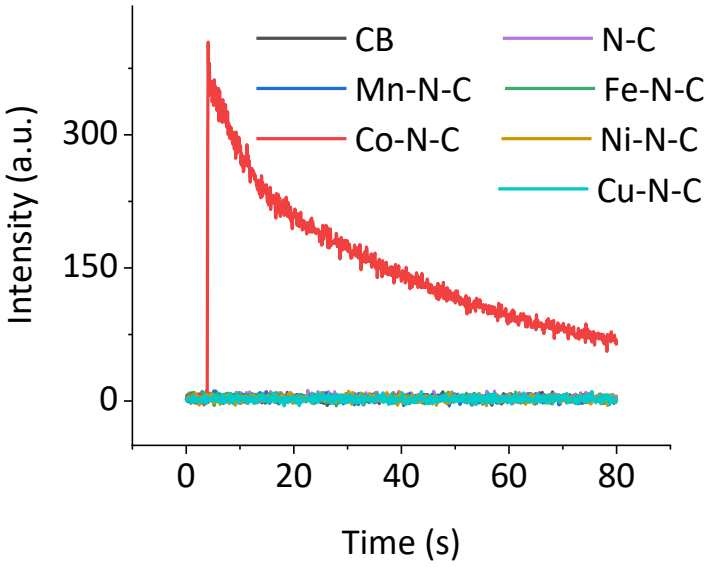

Figure S25. The chemiluminescence kinetic curves at 425 nm for monitoring the catalytic oxidation of 2.5 mM luminol with 250 mM H_2O_2 in the presence of 50 μg mL^{-1} CB, N-C AND M-N-C nanozymes in 0.01 M NaOH.

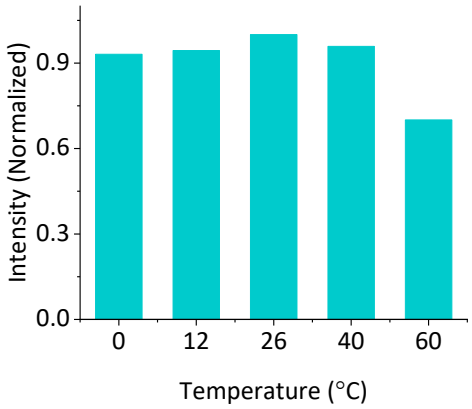

Figure S26. The temperature dependent activity of the catalytic oxidation of 2.5 mM luminol with 250 mM H_2O_2 in the presence of 50 mg mL^{-1} Co-N-C nanozymes in 0.01 M NaOH.

The catalytic activity of Co-N-C under different temperatures was also investigated. As shown in **Figure S26**, the catalytic activity of Co-N-C was almost unaffected when the temperature increased from 0 to 40 ℃, but decreased when the temperature further increased to 60 ℃.

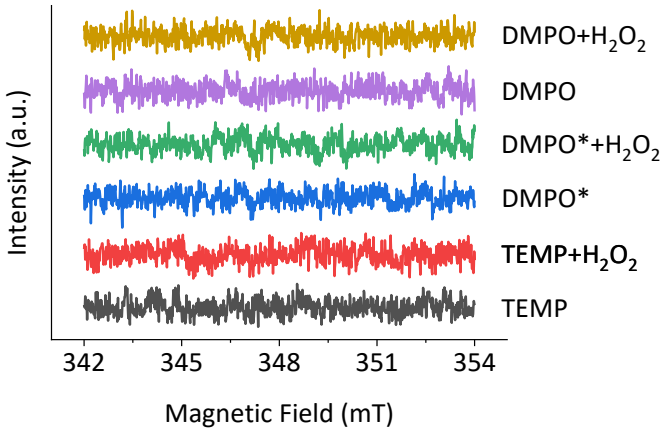

Figure S27. ESR spectra of spin trapping agent (TEMP, DMPO and DMPO*) and that with H_2O_2 in 0.1 M HAc-NaAc solution. * was represented in methanol solution.

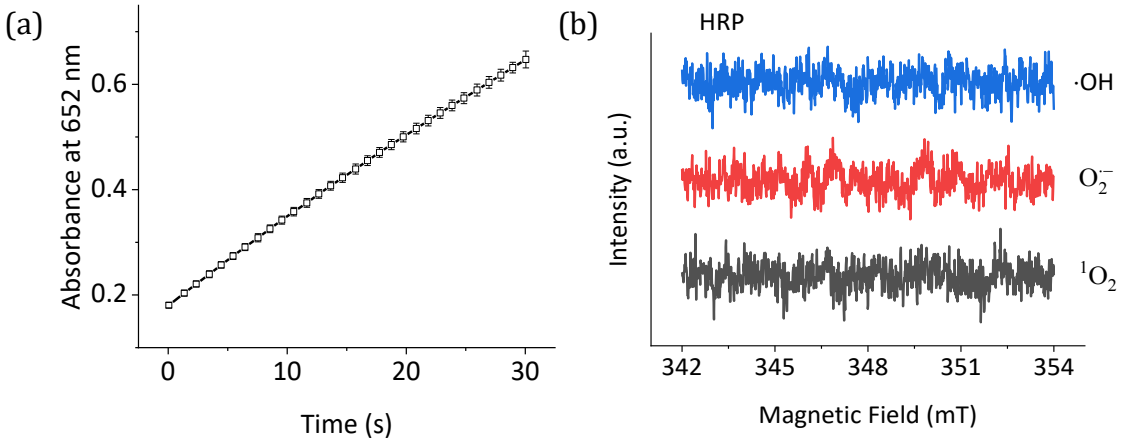

Figure S28. (a) The time evolution of adsorption at 652 nm for monitoring the catalytic oxidation of 1 mM TMB with 100 mM H_2O_2 in the presence of 20 ng mL^{-1} HRP in 0.1 M HAc-NaAc buffer solution (pH 3.6). (b) ESR spectra of spin adduct of hydroxyl radical, superoxide radical and singlet oxygen generated during activation of H_2O_2 by HRP in 0.1 M HAc-NaAc solution.

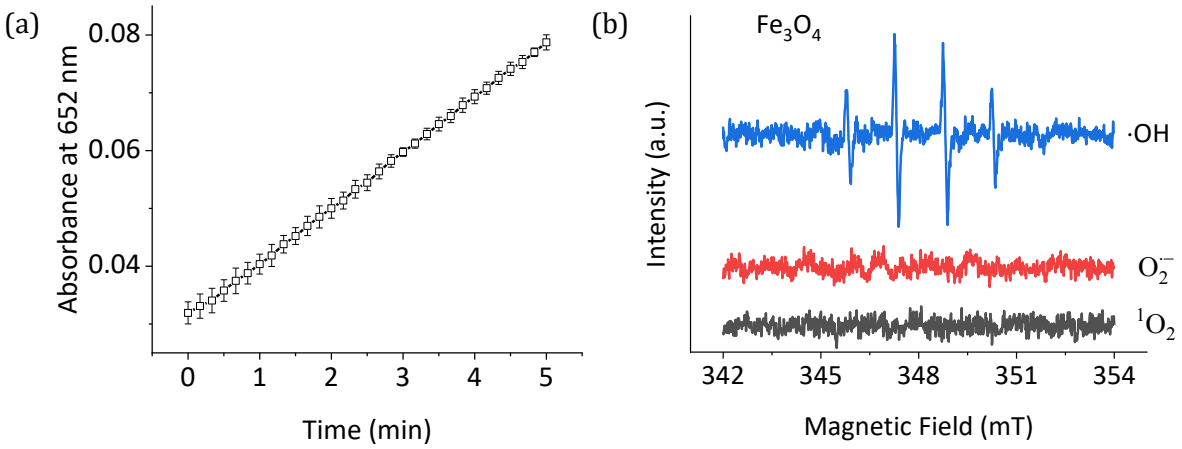

Figure S29. (a) The time evolution of adsorption at 652 nm for monitoring the catalytic oxidation of 0.5 mM TMB with 5 mM H_2O_2 in the presence of 10 μg mL^{-1} Fe_3O_4 in 0.1 M HAc-NaAc buffer solution (pH 3.6). (b) ESR spectra of the spin adduct of hydroxyl radical, superoxide radical, and singlet oxygen generated during activation of H_2O_2 by Fe_3O_4 in 0.1 M HAc-NaAc (pH 3.6).

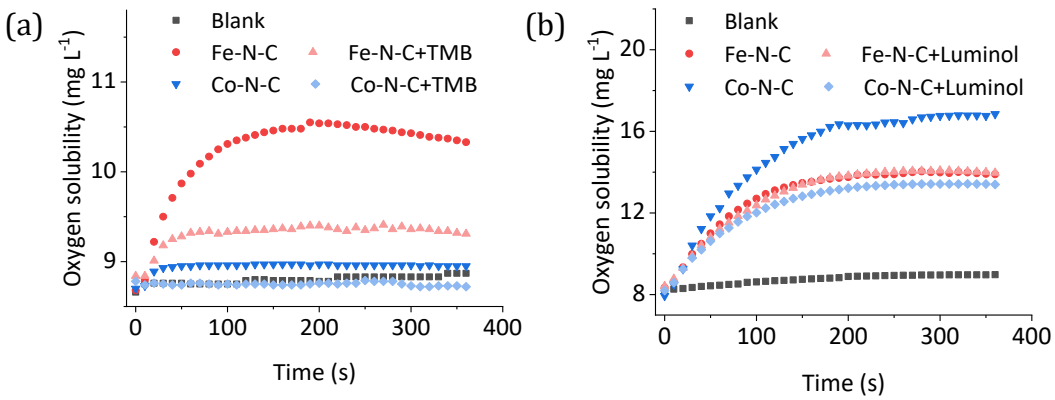

Figure S30. Influences of TMB and Luminol on the decomposition of H_2O_2 catalyzed by $M_{0.5}$-N-C (M = Fe, Co) in 0.1 M HAc-NaAc (a) and 0.01 M NaOH (b), respectively.

To verify the supposed competition between peroxidase- and catalase-like properties, the catalase-like property of M-N-C (M = Fe, Co) was studied by measuring the oxygen-generation ability in 0.1 M HAc-NaAc buffer solution. As shown in **Figure S30a**, the O_2 formation rate was significantly improved with the catalysis of Fe-N-C, while it decreased evidently when TMB was further added. In contrast, Co-N-C showed a negligible activity in the catalytic decomposition of H_2O_2. The catalase-like property of Co-N-C in an alkaline condition was also investigated in the oxidation of luminol. As shown in **Figure S30b**, O_2 was detected in the solution simultaneously containing H_2O_2 and Co-N-C. Nevertheless, the O_2 yield was inhibited when luminol, a stronger electron donor, was introduced to the solution. In contrast, at the identical conditions, Fe-N-C showed much lower activity in the catalytic decomposition of H_2O_2; meanwhile, the O_2 yield was negligibly influenced by introducing luminol (**Figure S30b**). In this context, Co-N-C catalyzed the oxidation of luminol with H_2O_2 also following the competition mechanism but variable in ROS affinity.

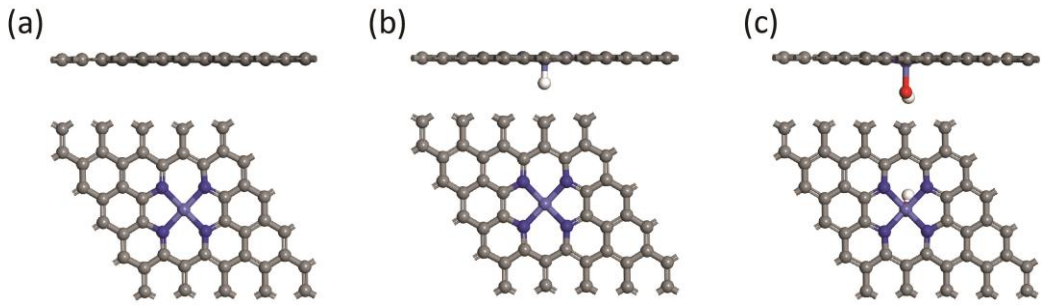

Figure S31. Optimized structures of M-N-C (a), H (b) and OH (c) adsorbed M-N-C. White, grey, blue, red and cyan balls represent H, C, N, O and M atoms, respectively. Unless otherwise specified, the type of atoms in the following structural models are the same. The E_{ads} of H on Fe-N-C and Co-N-C were -2.18 eV and -2.29 eV, respectively. The E_{ads} of OH on Fe-N-C and Co-N-C were-2.81 eV and -2.34 eV, respectively.

Taking Fe-N-C as an example, the excellent property of predominant Fe-N_4 was confirmed recently.[14] A leading postulate is that the iron-containing active sites exist primarily in a pyridinic Fe-N_4 ligation environment,[15] as molecular model catalysts generally feature pyrrolic coordination. There exist other M–N_x functionalities; however, previous computation proved the M-N_4 to be the dominating factor as compared to other M-N_x functionalities.[16] As such, to minimize the uncertainness, we adopted the well-developed synthesis method in **Ref. S10** for M-N-C.

Moreover, in this study, except for N coordinating to Fe, there are indeed other types of N, but which was proved not the main source of the catalytic activity of Fe-N-C (see more discussion on the high-resolution N 1s spectra of N-C and Fe-N-C in **Figure S14**, and their catalytic activity for the oxidation of TMB in **Figure 2c**). In addition, the types of N did not alter significant in different M-N-C (see more discussion on the high-resolution N 1s spectra in **Figure S15 & S16**). Thus, we speculate that all the metal ions have a similar fate during the pyrolyzing.

In these regards, the M–N_4 single active site model (**Figure S31a**) was selected as in theoretic calculations.

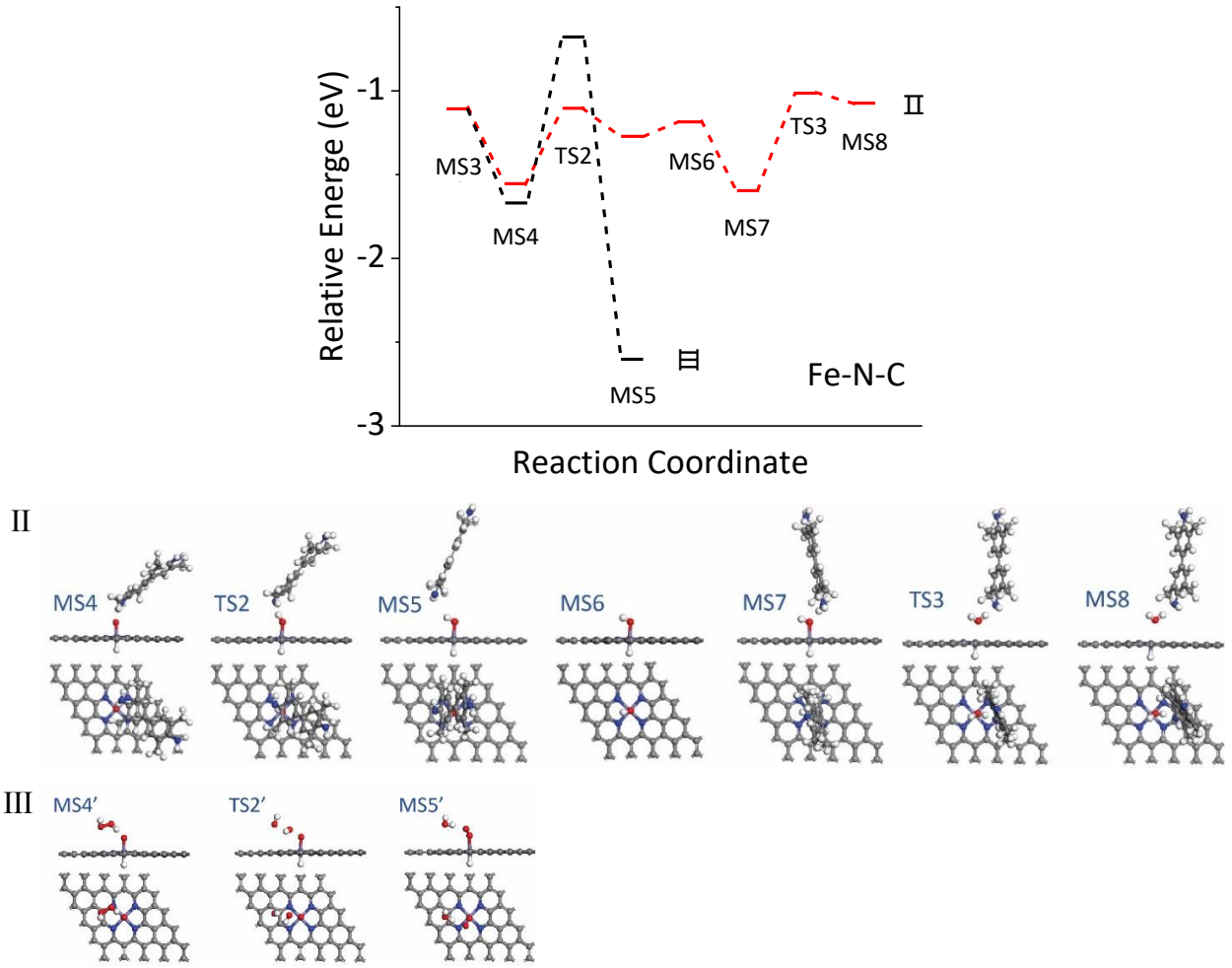

Figure S32. Free energy diagram of the oxidation of TMB (II) and H_2O_2 (III) and the corresponding reaction configurations of the MS and TS involved during the oxidation reactions.

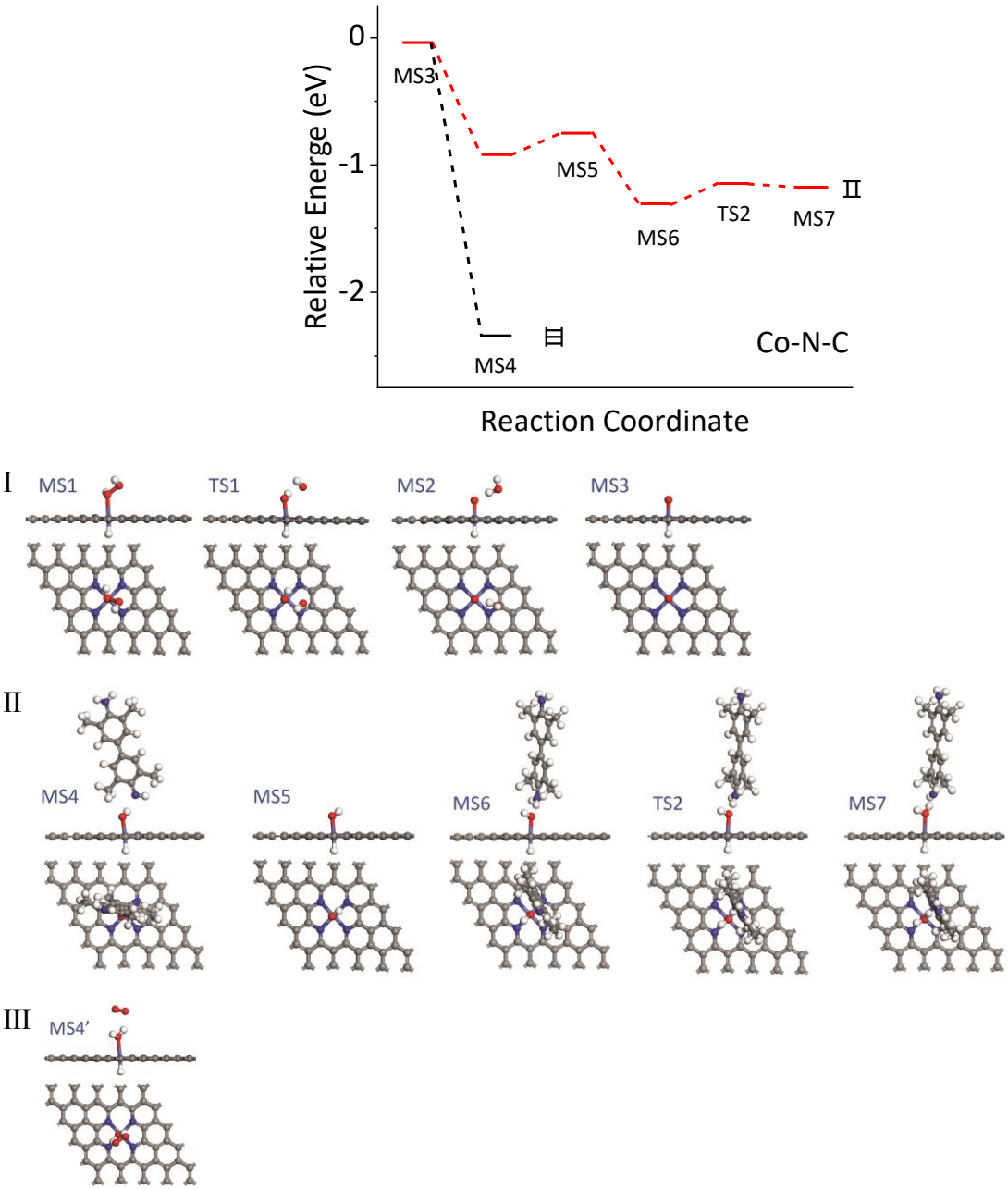

Figure S33. Free energy diagram of the oxidation of TMB (II) and H_2O_2 (III) and the corresponding reaction configurations of the MS and TS involved during the formation of Co=O (I) and the oxidation reactions. The first TMB was easily dissociated to the TMB_{ox} by N-H bond cleavage and transfer H to H adsorbed Co=O. The H_2O_2 was easily oxidized by transferring H to Co=O.

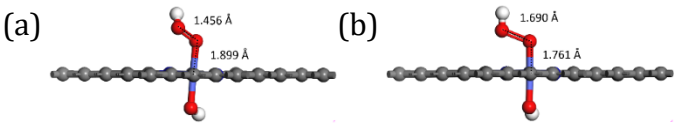

Figure S34. The corresponding structure and bond length of MS1 (a) and TS1 (b) involved during the formation of Co = O species on OH adsorbed Co-N-C. The obviously increased O-O bond length was observed in TS1 than in MS1, which was significant for the formation of Co = O species.

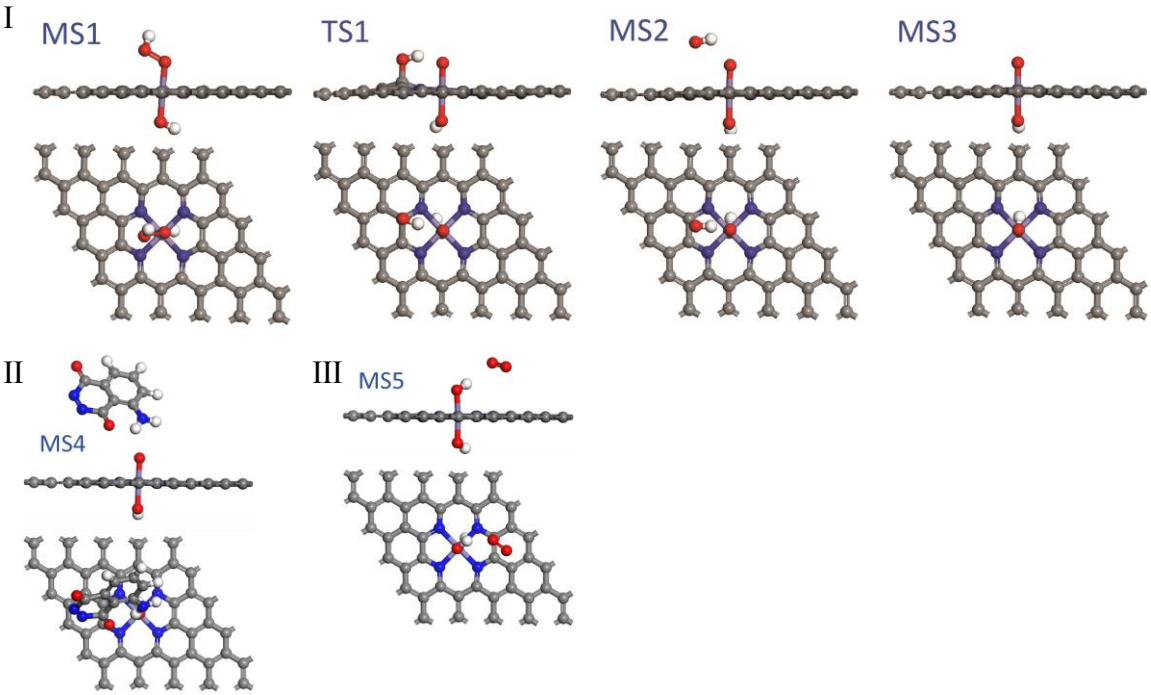

Figure S35. Reaction configurations of the MS and TS involved during the formation of Fe=O (I) and the optimized structure of Luminol adsorbed (II) and the second HO_2^- oxidation (III) on OH adsorbed Fe=O. The H of HO_2^- was easily transfer to OH adsorbed Fe=O species

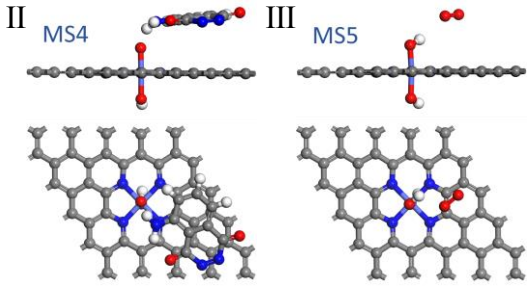

Figure S36. Optimized structures of Luminol adsorbed and the second HO_2^- oxidation on OH adsorbed Co=O species. The H of HO_2^- was easily transfor to Co=O species.

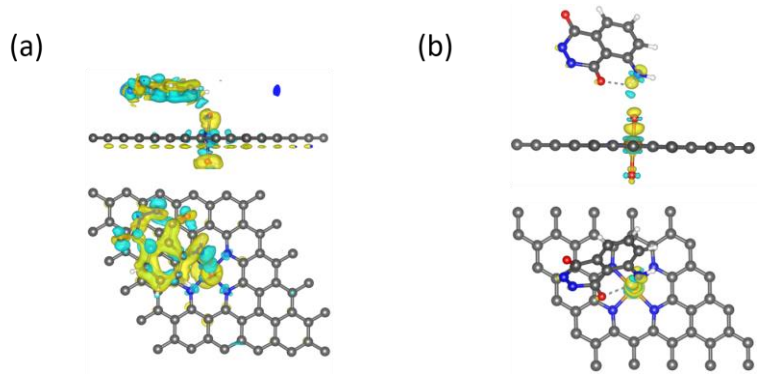

Figure S37. Top and side views of the differential charge density of luminol adsorbed on Co-N-C (a) and Fe-N-C (b). The blue and yellow regions represent charge loss and charge gain, respectively.

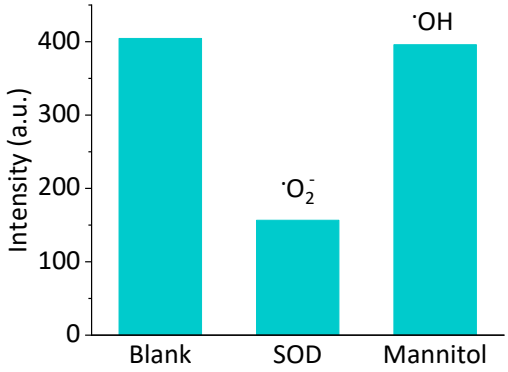

Figure S38. Effects of ROS scavengers on the oxidation of luminol with H_2O_2 catalyzed by $Co_{0.5}$-N-C in view of the chemiluminescence intensity at 420 nm.

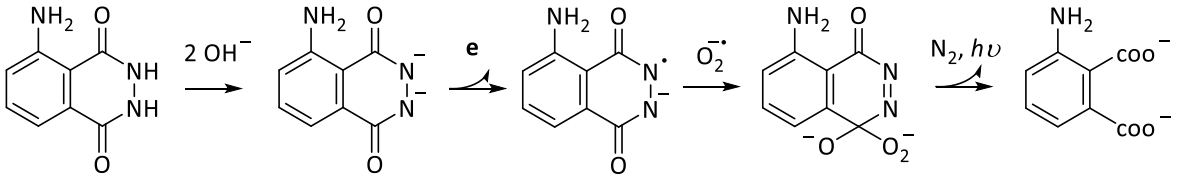

Figure S39. The possible mechanism of luminol oxidation.[17, 18]

Table S1. Specific surface area of N-C, all the Fe-N-C and Co-N-C nanozymes.

Sample	*SSA* ($m^2\ g^{-1}$)	SSA_M ($m^2\ g^{-1}$)	SSA_E ($m^2\ g^{-1}$)
CB	1199.328	1188.060	11.268
N-C	653.714	361.153	292.560
$Fe_{0.15}$-N-C	551.837	308.141	243.696
$Fe_{0.5}$-N-C	490.074	260.118	229.956
$Fe_{1.5}$-N-C	390.629	87.177	303.451
$Fe_{4.5}$-N-C	378.542	117.676	260.866
$Co_{0.5}$-N-C	440.893	77.916	362.977
$Co_{1.5}$-N-C	327.500	77.398	250.102
$Co_{4.5}$-N-C	448.549	121.246	327.303

SSA is the Brunauer-Emmet-Teller (BET) specific surface area; SSA_M is the micropore specific surface area and SSA_E is the external specific surface area based on the t-plot method.

The specific surface area of (Fe-)N-C calculated by the Brunauer-Emmet-Teller (BET) method decreased from 653.714 to 378.542 m^2/g with increasing the iron concentration (Fe_0-, $Fe_{0.15}$-, $Fe_{0.5}$-, $Fe_{1.5}$-, $Fe_{4.5}$-N-C) and far less than that of CB (1199.328 m^2/g), which may be attributed to the increased secondary graphene-like structure on the surface of graphene domains and inside the mesopores of CB support.

Table S2. The percentage of nitrogen species of N-C and M-N-C (M= Fe, Co, Mn, Ni and Cu) nanozymes.

	N_x-Metal and (or) imine (%)	Pyridinic-N (%)	Pyrrolic-N (%)	Graphitic-N (%)	Oxidized-N (%)
N-C	14.45	34.19	37.33	8.53	5.51
$Fe_{0.15}$-N-C	18.28	34.95	35.12	7.23	4.43
$Fe_{0.5}$-N-C	18.49	32.98	35.91	7.45	5.17
$Fe_{1.5}$-N-C	18.88	31.01	36.41	8.16	5.43
$Fe_{4.5}$-N-C	18.99	32.04	35.95	8.63	4.89
$Co_{0.5}$-N-C	18.04	33.74	34.69	8.32	5.22
$Co_{1.5}$-N-C	19.58	35.53	33.81	6.68	4.41
$Co_{4.5}$-N-C	19.72	29.15	36.00	9.13	6.00
$Mn_{0.5}$-N-C	20.03	34.55	32.90	7.84	4.68
$Ni_{0.5}$-N-C	20.01	34.90	32.74	7.30	5.04
$Cu_{0.5}$-N-C	16.76	36.43	34.47	7.16	5.18

Supporting Reference

1. G. Kresse and J. Furthmuller, *Comp. Mater. Sci.*, 1996, **6**, 15-50.
2. G. Kresse and J. Furthmuller, *Phys. Rev. B*, 1996, **54**, 11169-11186.
3. P. Hohenberg and W. Kohn, *Phys. Rev. B*, 1964, **136**, 864-871.
4. W. Kohn and L. J. Sham, *Phys. Rev.*, 1965, **140**, 1133-1138.
5. P. E. Blochl, *Phys. Rev. B*, 1994, **50**, 17953-17979.
6. J. P. Perdew, K. Burke and M. Ernzerhof, *Phys. Rev. Lett.*, 1996, **77**, 3865-3868.
7. H. J. Monkhorst and J. D. Pack, *Phys. Rev. B*, 1976, **13**, 5188-5192.
8. L. Z. Gao, J. Zhuang, L. Nie, J. B. Zhang, Y. Zhang, N. Gu, T. H. Wang, J. Feng, D. L. Yang, S. Perrett and X. Yan, *Nature Nanotechnology*, 2007, **2**, 577-583.
9. C. C. Ge, G. Fang, X. M. Shen, Y. Chong, W. G. Wamer, X. F. Gao, Z. F. Chai, C. Y. Chen and J. J. Yin, *ACS Nano*, 2016, **10**, 10436-10445.
10. P. Pachfule, D. Shinde, M. Majumder and Q. Xu, *Nat. Chem.*, 2016, **8**, 718-724.
11. B. Jiang, D. M. Duan, L. Z. Gao, M. J. Zhou, K. L. Fan, Y. Tang, J. Q. Xi, Y. H. Bi, Z. Tong, G. F. Gao, N. Xie, A. Tango, G. H. Nie, M. M. Liang and X. Y. Yan, *Nat. Protoc.*, 2018, **13**, 1506-1520.
12. X. Y. Wang, X. J. J. Gao, L. Qin, C. D. Wang, L. Song, Y. N. Zhou, G. Y. Zhu, W. Cao, S. C. Lin, L. Q. Zhou, K. Wang, H. G. Zhang, Z. Jin, P. Wang, X. F. Gao and H. Wei, *Nat. Commun.*, 2019, **10**, 704.
13. A. Kuchler, M. Yoshimoto, S. Luginbuhl, F. Mavelli and P. Walde, *Nat. Nanotech.*, 2016, **11**, 409-420.
14. H. T. Chung, D. A. Cullen, D. Higgins, B. T. Sneed, E. F. Holby, K. L. More and P. Zelenay, *Science*, 2017, **357**, 479-483.
15. T. Marshall-Roth, N. J. Libretto, A. T. Wrobel, K. J. Anderton, M. L. Pegis, N. D. Ricke, T. Van Voorhis, J. T. Miller and Y. Surendranath, *Nat. Commun.*, 2020, **11**, 5283.
16. W. Ju, A. Bagger, G. P. Hao, A. S. Varela, I. Sinev, V. Bon, B. Roldan Cuenya, S. Kaskel, J. Rossmeisl and P. Strasser, *Nat. Commun.*, 2017, **8**, 944.
17. M. Mayer, S. Takegami, M. Neumeier, S. Rink, A. Jacobi von Wangelin, S. Schulte, M. Vollmer, A. G. Griesbeck, A. Duerkop and A. J. Baeumner, *Angew. Chem. Int. Ed.*, 2018, **57**, 408-411.
18. K. Zhao, W. Shen and H. Cui, *J. Mater. Chem. C*, 2018, **6**, 6549-6555.